AMERICAN ACADEMY OF OPHTHALMOLOGY®

Automated Nonperfusion Quantification in Diabetic Retinopathy on Ultra-Widefield Swept-Source OCT Angiography

Tai Yong Loh, MBBS,[1,] Juling Sia, MBBS,[1,*] Wei Hing Seah, MBBS,[2] Lingyi Zhuang, MBBS,[1] Wenjun Song, M.Eng,[2] Yue Qiu,[3] Xiaofeng Shen, M.Eng,[3] Zhongqing Yu, M.Eng,[3] Ryan Tan, MBBS,[1] Nuo Tang, MBBS,[4] Yusra Asad, MBBS,[2] Colin Ming Hui Goh, MBBS,[1] Charmayne Xinyi Ang, MBBS,[1] Celyn Chng, MBBS,[1] Peiqi Lo, MBBS,[1] Pavan Paniharam, MBBS,[1] Ser Koon Goh, MBBS,[1] Hnin Hnin Oo, MBBS,[2] Min Wang, MD, PhD,[4] Rupesh Agrawal, MD,[1,2,5,6,7] Nicola Yi An Gan, MBBS,[2] Yali Jia, PhD,[8,9] Sandy Wenting Zhou, MD[1,2]*

Purpose: To evaluate the performance of a customized deep learning algorithm for automated segmentation of nonperfusion area (NPA) on ultra-widefield swept-source OCTA (UWF SS-OCTA) and its utility in diabetic retinopathy (DR) severity assessment.

Design: Cross-sectional study.

Subjects: A total of 180 eyes from 122 participants representing all grades of DR severity.

Methods: We developed a convolutional neural network based on a multiscale U-Net backbone with squeeze-and-excitation attention for segmentation of NPAs on en face SS-OCTA all-retinal-layer images from 3 scan patterns: 6 × 6 mm, 12 × 12 mm, and 29 × 24 mm. Ground-truth annotations of NPAs and nongradable area (NGA) on en face OCTA images were generated by 2 independent graders and adjudicated by a vitreoretinal specialist. A corresponding en face structural OCT image was incorporated to distinguish true NPAs from shadow artifacts. Segmentation outputs included NPA, NGA, and shadow artifacts. Pixel-level accuracy was assessed with the F1 score. Nonperfusion index (NPI) was defined as NPA/gradable area. The level of agreement between human-labeled and algorithm-predicted NPI was analyzed using Bland–Altman analysis.

Main Outcome Measures: Algorithm F1 score and NPI.

Results: The algorithm for NPA segmentation achieved a mean F1 score of 0.82 ± 0.01 in 6 × 6 mm, 0.84 ± 0.03 in 12 × 12 mm, and 0.83 ± 0.02 in 29 × 24 mm, with no significant difference across fields of view ($P = 0.12$). Algorithm-derived NPI strongly agreed with expert grading (intraclass correlation coefficient >0.979). Both human- and algorithm-derived NPI increased progressively with increased DR severity in all scan patterns demonstrated by the Kruskal–Wallis test (6 × 6 mm: human: $P = 0.02$; algorithm: $P = 0.03$; 12 × 12 mm: algorithm $P < 0.001$; human $P < 0.001$; 29 × 24 mm: algorithm: $P < 0.001$; human: $P < 0.001$) with the largest magnitude of increase in 29 × 24 mm scans. The algorithm for foveal avascular zone segmentation also achieved a mean F1 score of 0.88 ± 0.05 for 6 × 6 mm images and 0.85 ± 0.05 for 12 × 12 mm images.

Conclusions: This deep learning algorithm was validated on single-scan UWF SS-OCTA for automated NPA segmentation and quantification. It demonstrates high accuracy and scalability across multiple scan sizes, supporting its potential integration into objective DR OCTA biomarker analysis.

Financial Disclosure(s): Proprietary or commercial disclosure may be found in the Footnotes and Disclosures at the end of this article. *Ophthalmology Science 2026;6:101059*

Diabetic retinopathy (DR), the most common microvascular complication of diabetes mellitus, affects >100 million people worldwide and remains a leading cause of preventable blindness.[1] Early detection is critical to reduce the risk of vision-threatening complications.[2] Retinal nonperfusion area (NPA) is a well-established biomarker of DR progression, with fundus fluorescein angiography (FFA) studies demonstrating strong associations between NPA burden and disease severity.[3] However, FFA is an invasive and time-consuming procedure.[4] Moreover, although fluorescein leakage is useful for identifying neovascularization and intraretinal microvascular abnormalities in proliferative DR (PDR), it can obscure the boundaries of capillary dropout, thereby impeding accurate NPA quantification.[5]

Noninvasive imaging of NPA can be accomplished using OCT angiography (OCTA), which provides rapid 3-dimensional visualization of both retinal and choroidal vasculature.[5] Multiple studies comparing OCTA and FFA have reported a higher degree of accuracy in detection of NPA by OCTA,[6] while also being comparable to FFA in

https://doi.org/10.1016/j.xops.2025.101059
ISSN 2666-9145/26

detecting other DR biomarkers such as intraretinal microvascular abnormalities.[7] Yet, previous studies utilizing OCTA have been limited by a small field of view (FOV).[8] The recent development of ultra-widefield swept-source OCTA (UWF SS-OCTA) enables visualization of retinal vasculature beyond the posterior pole where NPAs tend to occur more frequently.[9] Because a greater peripheral NPA burden has been shown to be associated with increased risk of DR progression, this extended FOV has enhanced the clinical utility of NPA as a prognostic marker for DR.[10]

Deep learning–based approaches for automated NPA segmentation and quantification have demonstrated a high degree of accuracy in identifying NPA and differentiating them from shadow artifacts on OCTA.[11–15] Unlike rule-based approaches that identify NPA based on differences in intercapillary distance and signal-intensity thresholds, deep learning–based approaches can perform well across different scan sizes and image qualities because they learn subtle features of NPA morphology and surrounding vessels rather than following a strict set of rules. To date, most deep learning algorithms have been trained on narrow FOV OCTA and may miss clinically significant peripheral NPAs if deployed on ultra-widefield (UWF) images. Although image montaging can increase the effective FOV, it is time-consuming and technically challenging to perform consistently in actual clinical settings.[16,17] To our knowledge, no prior studies have developed and validated a deep learning algorithm for automated NPA segmentation and quantification on single-scan UWF SS-OCTA.

In this study, we developed a customized, artifact-aware deep learning algorithm for NPA segmentation across multiple OCTA scan sizes, including the largest available 29 × 24 mm field. We further evaluated its performance across DR severity stages and explored its potential clinical utility as a tool for reproducible biomarker quantification for disease grading and progression monitoring.

Methods

This prospective, cross-sectional study was conducted at a tertiary referral eye care center in Singapore, between November 2024 and September 2025. This study was approved by the Institutional Review Board of Tan Tock Seng Hospital and adheres to the Declaration of Helsinki. Written informed consent was obtained from all patients.

Study Population

Patients aged ≥18 years with type 1 or type 2 diabetes mellitus and a diagnosis of DR on dilated fundus examination were prospectively enrolled. Diabetic retinopathy severity was classified according to the International Clinical Diabetic Retinopathy (ICDR) Severity Scale. The exclusion criteria are as follows: tractional retinal detachment, history of panretinal photocoagulation, intravitreal injection, or vitrectomy; co-existing ocular diseases such as glaucoma; high myopia (>6.0 diopters); significant media opacity such as dense vitreous hemorrhage, visually significant cataract including nuclear sclerotic cataracts, and cortical cataracts above grade 2.

UWF SS-OCTA Imaging Protocol

All patients were imaged using a SS-OCTA system (VG200; Intalight Imaging Ltd) with 3 macula-centered scan sizes—6 × 6 mm, 12 × 12 mm, and 29 × 24 mm. The device employs a 1050-nm central wavelength SS laser with an A-scan rate of 200–400 kHz and a maximum retinal imaging depth of 9 mm. Key acquisition parameters for each FOV are summarized in Table 1. Scanning was performed by trained photographers, and repeat scans were performed where necessary to ensure good image quality.

Data Set Preparation

The all-retinal-layer (ARL) en face OCTA image was segmented for NPA analysis. Bulk eye movement artifacts and projection artifacts[18] were automatically removed using the device's in-built deep learning algorithm in the software. The corresponding ARL en face structural OCT scan was also retrieved to enable recognition of shadow artifacts such as from cataract, vitreous hemorrhage, or eyelashes.

Image Quality Assessment

Image quality was independently evaluated by 3 trained graders (T.Y.L, J.S, L.Z.). Images with signal strength score <7 were excluded. All en face ARL OCTA and OCT images were also screened for localized poor image quality that could interfere with accurate NPA identification. Poor image quality areas were further categorized into shadow artifacts, defocus artifacts, and segmentation errors.

Shadow artifacts appear as flow-void areas on the angiogram with corresponding hyporeflectivity on the structural image, which commonly arise from overlying opacities (e.g., lid/lashes, floaters, vitreous hemorrhage, superficial hyperreflective lesion, vignetting, or poor contact) producing reduced OCT reflectance.[19] Defocus artifacts, in contrast, manifest as loss of small capillaries on the angiogram corresponding to the out-of-focus region of the retina without any corresponding hypotransmission on the structural image.[19] Segmentation errors refer to misidentification of retinal boundaries.[19] If 2 of the 3 graders (≥2/3) judged that these poor image quality areas affected more than one-third of the total image area, the image was deemed *poor quality* and excluded from further analysis.

Manual Annotation and Ground-Truth Definition

After exclusion of poor-quality images, manual segmentation was performed by two graders (T.Y.L. and J.S.) and confirmed by a vitreoretinal faculty (S.W.Z.). When artifacts occupied less than one-third of the image, regions containing defocus artifacts or segmentation errors were manually labeled as "nongradable areas (NGA)" on the en face OCTA image. Shadow artifacts were not manually labeled, as they were subsequently detected using the corresponding structural image through the deep learning algorithm (Fig 1A).

Nonperfusion area segmentation was performed only within gradable regions, using the raw en face OCT image to differentiate true NPAs from shadow artifacts. Each paired OCTA (with NPA + NGA segmentation) and structural image (Fig 1A–B) was then used as input for model training.

Table 1. Scan Patterns of OCTA Device across Multiple Fields of View

Field of View	Number of A-Scans per B-Scan	Number of B-Scan Locations per Volume Scan	Spacing between Adjacent A-Scans or B-Scans
6 × 6 mm	512	512	11.7 μm
12 × 12 mm	1024	1024	11.7 μm
29 × 24 mm	1536	1240	19 μm

OCTA = OCT angiography.

For ground-truth labeling, an NPA was defined as a contiguous region of absent flow signal bounded by discrete vessel borders in the absence of structural en face OCT changes.[14] A threshold area was applied to minimize false-positives from physiological intercapillary gaps determined empirically from healthy control scans as the largest misclassified intercapillary region. The minimum threshold was 278 pixels (0.038 mm^2) for 6 × 6 mm images, 213 pixels (0.11 mm^2) for 12 × 12 mm images, and 248 pixels (0.25 mm^2) for 29 × 24 mm images.

The foveal avascular zone (FAZ) was also labeled in 6 × 6 mm and 12 × 12 mm scans because it constitutes a physiologic nonperfusion zone and visually resembles true NPAs, thereby improving the model's ability to discriminate between the 2. The FAZ was omitted from 29 × 24 mm labeling because it is small relative to total scan area, which contributes to reduced vascular resolution in the FAZ periphery. Model outputs comprised segmentation masks of NPA, NGA, and shadow artifacts on en face ARL OCTA images (Fig 1E).

Model Architecture

We designed a dual-encoder multimodal convolutional neural network to segment NPAs and NGAs on OCTA images. The architecture employs 2 Res-Net 34 encoders, separately

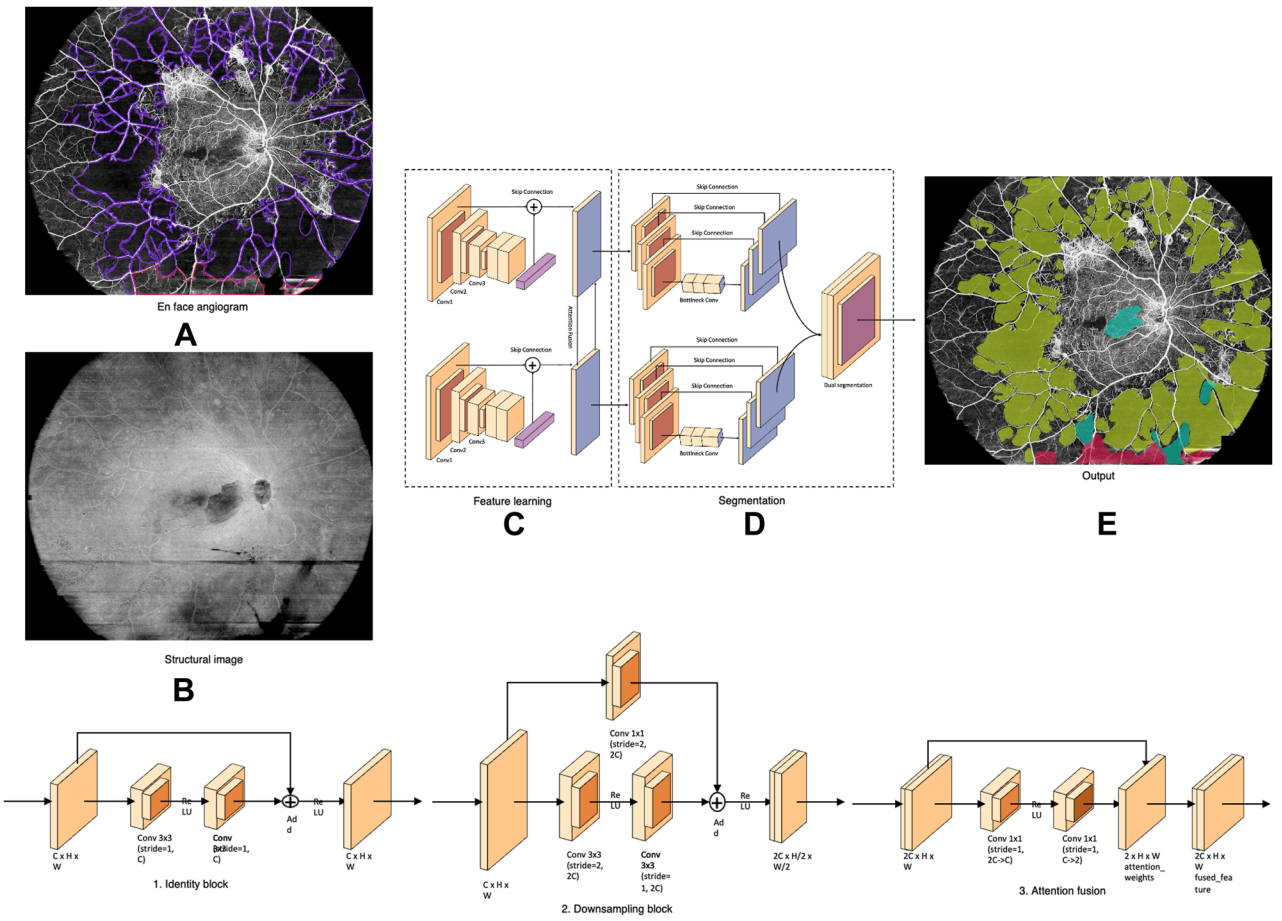

Figure 1. Illustration of model training using a multimodal fusion deep network architecture. (**A**) En face ARL OCTA image with segmented NPA (purple) and NGAs (red). (**B**) Corresponding raw structural en face OCT image. (**C** and **D**) Summary of model architecture. (**E**) Model output en face ARL OCTA showing NPA predictions (green), NGA predictions (red) and signal-intensity related artifacts (blue). ARL = all retinal layer; NGA = nongradable area; NPA = nonperfusion area; OCTA = OCT angiography.

processing en face ARL OCTA (Fig 1A) and en face structural OCT images (Fig 1B) to capture complementary vascular and structural features. Residual identity (Fig 1.1) and downsampling blocks (Fig 1.2) ensure progressive abstraction while preserving spatial consistency. Our contribution introduces hierarchical feature fusion at multiple encoder stages through an attention fusion module (Fig 1.3). This adaptive mechanism emphasizes discriminative features from each modality while suppressing redundancy, maintaining computational efficiency, and ensuring robust gradient propagation for joint optimization of dual segmentation targets. A 5-level U-Net decoder with transposed convolutions and skip connections reconstructs spatial detail, while a dual-channel segmentation head generates probability maps for NPAs and NGAs. These are refined by adaptive thresholding to yield binary outputs. By explicitly modeling NGAs, the network reduces ambiguity and improves distinction between pathological nonperfusion and imaging artifacts, thereby enhancing the reliability of OCTA-derived retinal biomarkers and their clinical interpretability.

Evaluation of Algorithm Performance

To ensure a rigorous and unbiased evaluation, algorithm performance was assessed using fivefold cross-validation at the patient level, such that each patient contributed data to only onefold. The data set was randomly divided into 5 mutually exclusive subsets of approximately equal size, maintaining proportional representation of DR severity levels within each fold.

In each iteration, fourfolds were used for training and one for validation. The model was trained from scratch in each cycle, and all reported results represent the mean performance across the 5 validation sets, ensuring robust estimation of model stability and generalizability.

Algorithm accuracy for NPA segmentation was quantified using the F1 score, which balances precision and recall at the pixel level. For each image, the F1 score was computed according to Equation 1:

$$F1 = \frac{2TP}{2TP + FP + FN} \qquad \text{Equation 1}$$

Equation 1: definition of F1 score where TP refers to true-positives—the number of pixels that were correctly identified by the model as NPA; FP refers to false-positives—the number of pixels that were incorrectly identified as NPA; and FN refers to false-negatives—the number of pixels of nonperfusion that were not identified by the model as NPA. The overall model performance was reported as the mean and standard deviation across all 5 validation sets, providing a robust assessment of the model's stability and generalization ability.

The final F1 score for each fold was averaged across all images before cross-fold aggregation. This approach provided a robust measure of the model's overall segmentation accuracy.

To evaluate quantitative accuracy, an independent expert grader (W.H.S.) manually annotated NPA regions of the images in the data set. The resulting nonperfusion index (NPI) values—defined as the ratio of NPA area to total gradable retinal area (Equation 2)—were compared between human and algorithm-derived results.

$$NPI = \frac{total\ NPA}{gradable\ retinal\ area} \qquad \text{Equation 2}$$

Equation 2: definition of NPI, where the total gradable retinal area (in pixels) is the sum of the pixels in each image after deduction of the total nongradable retinal area (in pixels).

This dual approach ensured both segmentation accuracy (via F1 score) and quantification reliability (via NPI concordance) were rigorously validated.

Statistical Analysis

All statistical analyses were performed using *R* (version 4.5.0, R Foundation for Statistical Computing) and *Python* (version 3.10.16, TensorFlow/PyTorch framework; Python Software Foundation). Continuous variables were summarized as mean ± standard deviation, and categorical variables as counts and percentages. Mixed-effects covariate analysis was performed to account for the use of both eyes from participants as well as demographic variations. Diabetic retinopathy severity, age, gender, and comorbidities such as hypertension, hyperlipidemia, ischemic heart disease, cerebrovascular accident, and chronic kidney disease were included as fixed effects. Because some participants had >1 eye analyzed, each participant was specified as a random intercept, and "eye" was treated as a repeated measure nested within each participant. Group comparisons were performed using the Kruskal–Wallis test for nonparametric data. When significant differences were detected ($P < 0.05$), Dunn post hoc test was applied for pairwise comparisons. Bland–Altman analysis was used to assess systematic bias and 95% limits of agreement (LOA), while intraclass correlation coefficients (ICCs) were computed to quantify absolute agreement.

Results

A total of 248 OCTA images from 180 eyes (122 participants) were analyzed in this study, comprising 63 (6 × 6 mm), 87 (12 × 12 mm), and 98 (29 × 24 mm) scans. Detailed demographics including age, gender, severity of DR, status of diabetic macular edema, and other comorbidities are summarized in Table 2.

Algorithm Performance across Scan Sizes

The deep learning algorithm achieved a mean F1 score of 0.82 ± 0.01 for 6 × 6 mm scans, 0.84 ± 0.03 on 12 × 12 mm scans, and 0.83 ± 0.02 for 29 × 24 mm scans, with no significant differences across FOVs ($P = 0.12$).

Performance across DR Severity

In UWF 29 × 24 mm images, the algorithm's F1 score increased with DR severity ($P = 0.004$), showing significant pairwise differences between mild–moderate nonproliferative DR (NPDR) versus severe NPDR ($P = 0.002$) and PDR ($P = 0.01$). No significant differences were observed across DR severity in 6 × 6 mm ($P = 0.87$) or 12 × 12 mm ($P = 0.71$) scans (Table 3). Representative segmentation outputs across severity levels and scan sizes are shown in Figure 2.

Covariate Analysis of Baseline Demographics and Comorbidities

Covariate analysis (Table 4) showed that NPI was not significantly influenced by variations in demographics such as age and gender, or comorbidities including presence of hypertension, hyperlipidemia, ischemic heart disease, cerebrovascular accident, or chronic kidney disease.

Table 2. Patient Demographics

Field of View	6 x 6 mm			12 x 12 mm			29 x 24 mm		
DR Severity	*Mild–mod NPDR*	*Severe NPDR*	*PDR*	*Mild–mod NPDR*	*Severe NPDR*	*PDR*	*Mild–mod NPDR*	*Severe NPDR*	*PDR*
No. of eyes	25	11	27	39	16	32	35	36	27
No. of patients	20	7	19	24	9	20	25	27	20
Male, n (%)	14 (70%)	4 (57%)	12 (63%)	18 (75%)	6 (67%)	16 (80%)	19 (76%)	17 (73%)	10 (50%)
Age, mean (SD)	58.65 (9.83)	60.56 (14.61)	58.40 (10.40)	60.00 (10.10)	61.15 (13.13)	55.80 (12.58)	57.08 (10.50)	58.87 (11.10)	52.45 (11.21)
Eyes with DME	9	6	13	7	7	18	-	-	-
Patients with HTN	16	7	15	23	11	25	25	16	14
Patients with HLD	18	7	17	27	11	19	26	16	17
Patients with IHD	0	1	4	4	6	3	0	9	3
Patients with CVA	4	3	2	1	2	1	4	3	1
Patients with CKD	1	1	5	2	0	3	7	6	3

CKD = chronic kidney disease; CVA = cerebrovascular accident; DME = diabetic macular edema; DR = diabetic retinopathy; HLD = hyperlipidemia; HTN = hypertension; IHD = ischemic heart disease; Mild–mod = mild–moderate; NPDR = nonproliferative diabetic retinopathy; PDR = proliferative diabetic retinopathy; SD = standard deviation.
Diabetic macular edema status was only collected for patients undergoing 6 × 6 mm and 12 × 12 mm scans as it primarily affects foveal avascular zone calculations.

FAZ Segmentation

For FAZ detection, the algorithm achieved mean F1 scores of 0.88 ± 0.05 (6 × 6 mm) and 0.85 ± 0.05 (12 × 12 mm). A significant difference was observed across DR severity in 6 × 6 mm scans ($P = 0.01$) but not in 12 × 12 mm scans ($P = 0.87$). Post hoc analysis confirmed this difference was limited to mild–moderate NPDR versus PDR eyes ($P = 0.006$).

Agreement between Algorithm and Human Grader for NPI

Bland–Altman analysis demonstrated excellent agreement between algorithm-predicted and human-graded NPA sizes with narrow LOA (Fig 3A, B and C). The algorithm slightly underestimated NPA for 6 × 6 mm (mean difference = −0.008; 95% LOA: −0.020 to 0.005) and 29 × 24 mm scans (mean difference = −0.002; 95% LOA: −0.010 to 0.005), and slightly overestimated NPA for 12 × 12 mm scans (mean difference = 0.0008; 95% LOA: −0.005 to 0.007). Despite these minor systematic biases, ICCs showed near-perfect agreement across all scan sizes (6 × 6 mm: ICC = 0.990; 12 × 12 mm: ICC = 0.979; 29 × 24 mm: ICC = 0.999).

NPI Correlation with DR Severity

The human-grader labeled and algorithm-derived NPIs demonstrated a significant gradual increase with DR severity across all 3 scan sizes (6 × 6 mm: algorithm: $P = 0.03$; human: $P = 0.02$; 12 × 12 mm: algorithm: $P < 0.001$; human: $P < 0.001$; 29 × 24 mm: algorithm: $P < 0.001$; human: $P < 0.001$, Fig 4). The largest incremental change in NPI was observed in 29 × 24 mm scans, where peripheral nonperfusion was most evident. Table 5 summarizes the algorithm-predicted NPI across DR severity levels for 3 scan sizes (6 × 6, 12 × 12, and 29 × 24 mm). In 6 × 6 mm scans, NPI differed significantly only between mild–moderate NPDR versus PDR ($P = 0.01$); however, the differences for mild–moderate versus severe NPDR ($P = 0.12$) and severe NPDR versus PDR ($P = 0.63$) were not significant. In 12 × 12 mm scans, NPI was significantly different for mild–moderate NPDR versus severe NPDR ($P < 0.001$) and mild–moderate NPDR versus PDR ($P < 0.001$), but not for severe NPDR versus PDR ($P = 0.24$). In contrast, all pairwise comparison of NPI between different severities of DR in 29 × 24 mm scans (UWF) were significant—mild–moderate NPDR versus severe NPDR ($P < 0.001$), mild–moderate NPDR versus PDR ($P < 0.001$), and severe NPDR versus PDR ($P = 0.02$).

FAZ Quantification

The mean predicted FAZ area was 0.35 mm^2, 0.33 mm^2, and 0.35 mm^2 for 6 × 6 mm images and 0.38 mm^2, 0.38 mm^2, and 0.32 mm^2 for 12 × 12 mm images across mild-moderate NPDR, severe NPDR, and PDR eyes, respectively. No significant differences in FAZ area were observed between severity grades for either scan size (6 × 6 mm, $P = 0.83$; 12 × 12 mm, $P = 0.29$).

Table 3. Algorithm Performance on OCTA Images across Varying FOVs and DR Severity

Field of view	F1 scores across DR severity			Overall F1 Score	*P* Value
	Mild—moderate NPDR	*Severe NPDR*	*PDR*		
6 x 6 mm	0.81 ± 0.03	0.84 ± 0.03	0.84 ± 0.03	0.82 ± 0.01	0.87
12 x 12 mm	0.80 ± 0.05	0.80 ± 0.09	0.84 ± 0.03	0.84 ± 0.03	0.83
29 x 24 mm	0.80 ± 0.05	0.82 ± 0.02	0.86 ± 0.03	0.83 ± 0.02	0.004

DR = diabetic retinopathy; FOV = field of view; NPDR = nonproliferative diabetic retinopathy; OCTA = OCT angiography; PDR = proliferative diabetic retinopathy.

Discussion

The study presents a novel, artifact-aware deep learning algorithm for automated segmentation and quantification of NPA across multiple scan protocols of UWF SS-OCTA, including the largest single-scan FOV currently available—29 × 24 mm. To our knowledge, this is the first validated deep learning algorithm capable of NPA segmentation across different scan sizes within a single architecture, with consistent performance across FOVs (mean F1 ≥0.82). The algorithm also integrates artifact recognition, NGA detection, and FAZ discrimination—critical steps for ensuring robust quantification in a clinical setting.

Several studies have demonstrated good agreement and strong correlations between NPA quantified on widefield OCTA and FFA, particularly for the detection of peripheral nonperfusion in DR.[20,21] Building on this prior work, our findings show that OCTA-derived NPI stratifies DR severity with high diagnostic performance. The increasingly extended FOV achievable with UWF OCTA, together with its rapid, dye-free, and noninvasive nature, makes OCTA an attractive and increasingly strong competitor to FFA for routine DR assessment and screening work. Several deep learning algorithms published so far based on FFA showed an accuracy ranging from 0.48 to 0.57.[22,23] However, a direct comparison of our algorithm's performance on OCTA and FFA is challenging because of the inherent differences between the 2 modalities (dye-based vs flow-based imaging, leakage vs nonleakage) and the resulting differences in NPA appearance and segmentation.

Prior studies have demonstrated the feasibility of deep learning for NPA segmentation on OCTA. Le Boite et al[24] reported an F1 score of 0.78 for NPA segmentation in 12 × 12 mm images. One key methodological difference

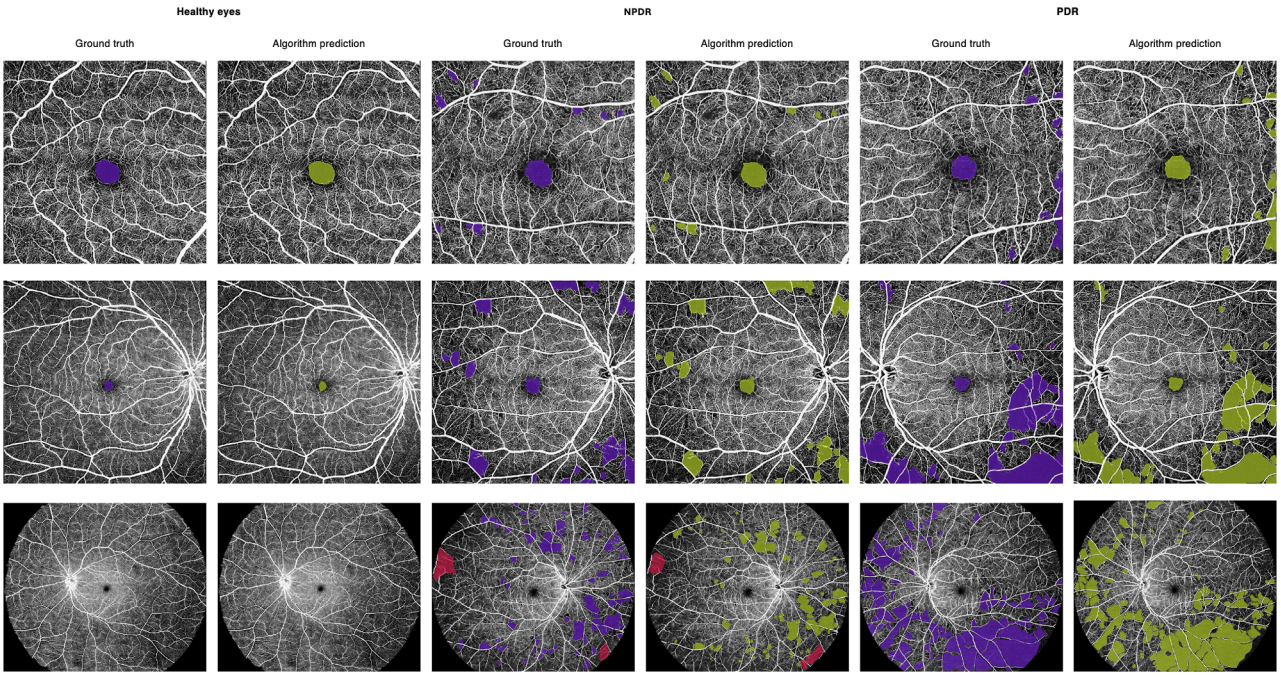

Figure 2. Nonperfusion area segmentation on OCTA images of varying DR severity grading. The top row shows 6 × 6 mm images, the middle row shows 12 × 12 mm images, while the 29 × 24 mm images are displayed in the bottom row. Manually segmented NPA and algorithm segmented NPA are denoted in purple and green, respectively, while manually segmented NGA and algorithm segmented NGA are denoted in red and orange, respectively. An increase in NPA with worsening DR severity grading is shown. DR = diabetic retinopathy; NGA = nongradable area; NPA = nonperfusion area; NPDR = nonproliferative diabetic retinopathy; OCTA = OCT angiography; PDR = proliferative diabetic retinopathy.

Table 4. Covariate Analysis of Effect of Baseline Variables on NPI

Baseline Variables	Coefficient (95% CI)	*P* Value
Age	0.001 (0, 0.002)	0.12
Gender	0.014 (−0.015, 0.042)	0.37
HTN	0.001 (−0.018, 0.020)	0.91
HLD	0.003 (−0.019, 0.024)	0.82
IHD	0 (−0.029, 0.022)	0.78
CVA	−0.028 (−0.058, 0.002)	0.07
CKD	0.023 (−0.002, 0.050)	0.08

CI = confidence interval; CKD = chronic kidney disease; CVA = cerebrovascular accident; HLD = hyperlipidemia; HTN = hypertension; IHD = ischemic heart disease; NPI = nonperfusion index.

is that their study defined low-quality regions solely by abrupt signal changes on the en face OCTA and did not distinguish between different types of artifacts. In contrast, our study specifically adopted a dual-channel multimodal convolutional neural network approach which incorporated reflectance changes on the structural layer to identify shadow artifacts. Other low-quality areas such as defocus artifacts and segmentation errors without corresponding hypotransmission changes on the structural layer were labeled separately as NGAs on the en face OCTA. This distinction reflects the fact that shadow artifacts present with absent flow signal on the angiogram and a corresponding hyporeflective area on the structural layer, whereas other artifact types do not present with

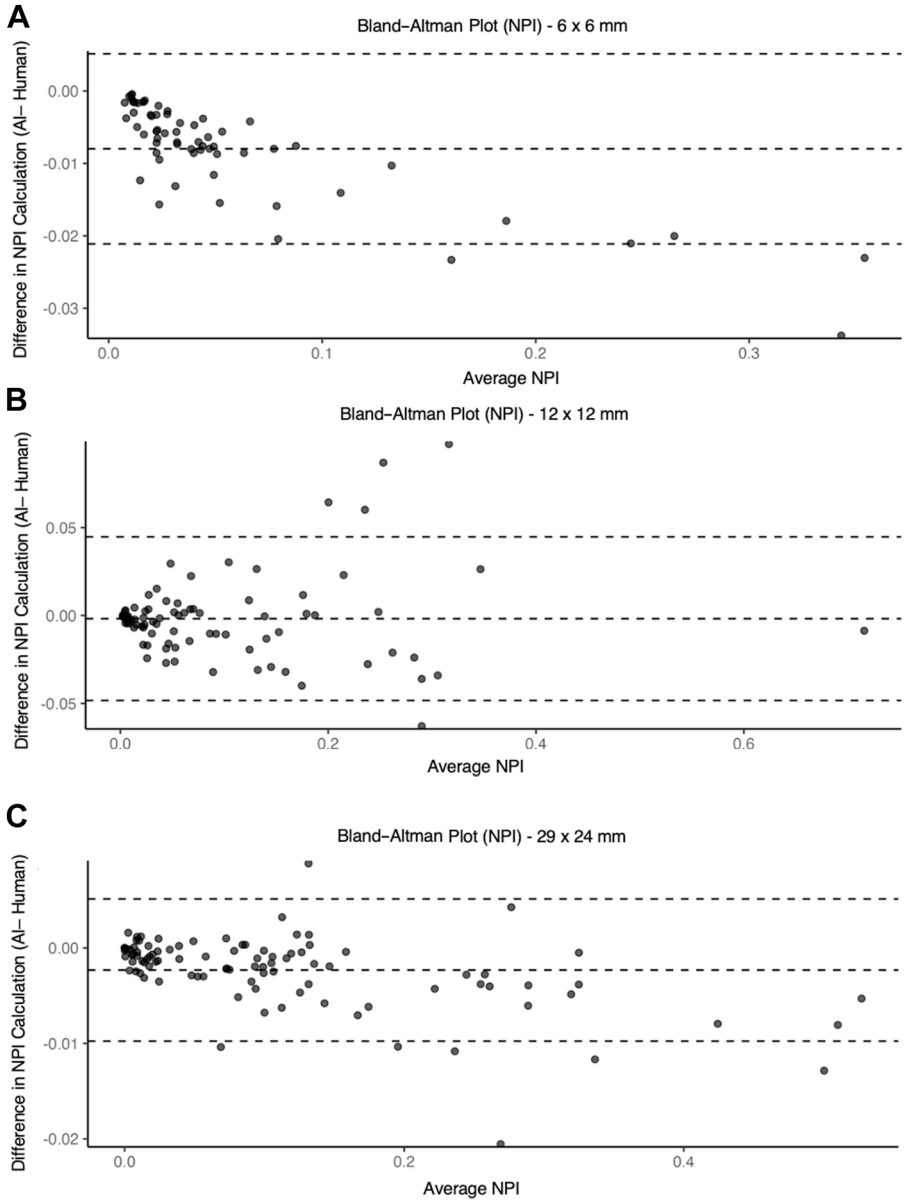

Figure 3. A, **B** and **C,** Bland–Altman plots for 6 × 6 mm, 12 × 12 mm, and 29 × 24 mm images, respectively, which show good agreement between ground truth and algorithm-predicted NPI despite statistically significant proportional bias. AI = artificial intellignece; NPI = nonperfusion index.

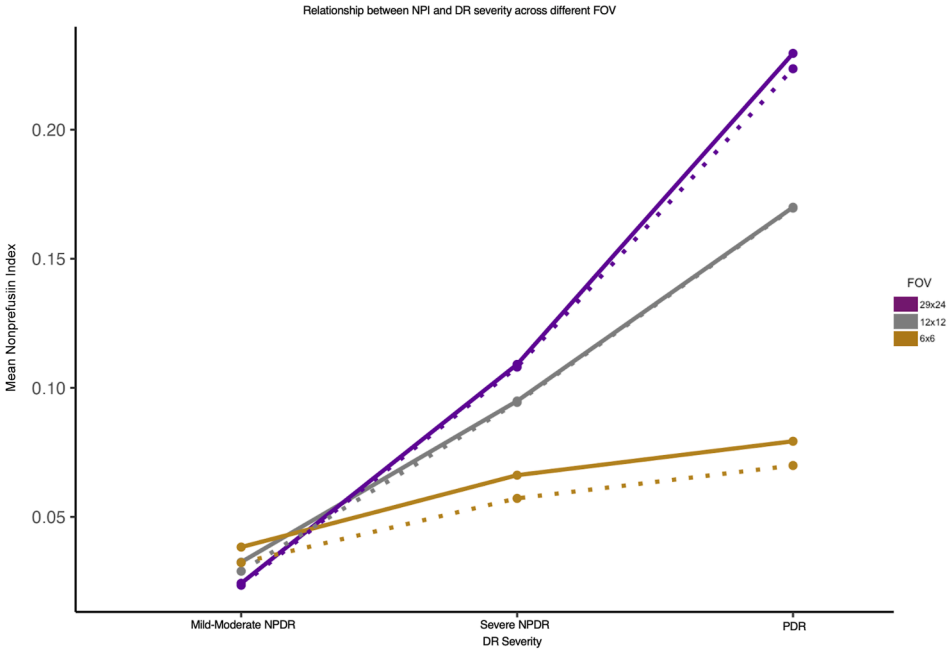

Figure 4. Line graph showing an increase in NPI with DR severity across all 3 FOVs (6 × 6 mm: $P = 0.03$, 12 × 12 mm: $P < 0.001$, 29 × 24 mm: $P < 0.001$). The solid line represents NPI derived from ground truth, while the dotted line represents NPI derived from the algorithm. The magnitude of increase in NPI was the most significant in 29 × 24 mm images and the least significant in the 6 × 6 mm images. There is minimal difference in between NPI calculated from ground truth and algorithm prediction across all 3 FOVs. DR = diabetic retinopathy; FOV = field of view; NPDR = nonproliferative diabetic retinopathy; NPI = nonperfusion index; PDR = proliferative diabetic retinopathy.

hypotransmission on both the OCTA and structural OCT concurrently.[19] Another deep learning algorithm described by Guo et al[14,15] uses 3 channels as input—namely the en face images, reflectance OCT image, and the retinal thickness maps, and their algorithm was trained on 17 × 6 mm montaged widefield scans of the nasal, temporal, and macula area.[14,15] It should be noted that montaged scans are subjected to less peripheral signal attenuation because of a higher sampling density and lower incidence of vignetting artifacts, which may make automated NPA detection on montaged scans less challenging than single-shot UWF OCTA scans. However, montaged scans are less practical for clinical application as it is a time-consuming process that requires multiple scans over longer periods of time that patients are sometimes unable to tolerate. This frequently results in greater patient eye movement and blinking that can generate motion artifacts and impair image quality.[19] The need to align images in montaged scans also leads to alignment errors that affect accurate quantification of NPAs.[14,25] Our study addresses this limitation by utilizing single-scan UWF images that reduces scan times and patient discomfort.

Apart from being the first to support NPA segmentation on single-scan UWF images, our deep learning algorithm is also the first to perform equally well across 3 different FOVs. The 6 × 6 mm and 12 × 12 mm FOVs were chosen as they represent the most widely used commercially available OCTA scanning protocols in DR research[26–29] and correspond to key regions of interest for macular and wider-field analysis in previous DR studies.[30,31] Although cross-device validation is still currently not possible due to variations in data sets and device specifications, comparisons of our algorithm performance with previous studies show that our algorithm is on par with previous FOV-specific algorithms. Guo et al reported F1 scores ranging from 0.82 ± 0.08 to 0.87 ± 0.10 for NPA

Table 5. Nonperfusion Index Values across Different Severities of DR and Scan Sizes

	Mean NPI (95% CI)		
	6 x 6 mm	*12 x 12 mm*	*29 x 24 mm*
Mild–moderate NPDR	0.032 (0.012–0.052)	0.029 (0.013–0.044)	0.024 (0.012–0.035)
Severe NPDR	0.057 (0–0.12)	0.094 (0.059–0.13)	0.11 (0.083–0.13)
PDR	0.069 (0.039–0.10)	0.17 (0.12–0.22)	0.22 (0.17–0.28)

CI = confidence interval; DR = diabetic retinopathy; NPDR = nonproliferative diabetic retinopathy; NPI = nonperfusion index; PDR = proliferative diabetic retinopathy.

segmentation on 6 × 6 mm images of eyes with DR, while Le Boite et al reported F1 score of 0.781 for NPA segmentation on 15 × 15 mm images. Although we are unable to directly compare UWF scan performance, as there are no previous deep learning algorithms for single-scan UWF images, a substitute comparison with 17 × 6 mm montaged WF scan reported by Guo et al, which reported an average F1 score of 0.79 ± 0.06 for mild−moderate NPDR and 0.78 ± 0.05 for severe NPDR and PDR images, shows that our algorithm achieved high performance without needing montaged scans.

Algorithm performance was also evaluated with Bland−Altman analysis and ICC, which both showed strong agreement of algorithm-predicted NPI with an expert human grader. The Bland−Altman analysis showed a slight underestimation in NPA area by the algorithm in 6 × 6 mm and 29 × 24 mm images and overestimation in 12 × 12 mm images. However, the difference is likely negligible for quantification in the clinical context. The high ICC values across all 3 FOVs further underscore the agreement between algorithm-predicted NPI with human-predicted NPI. Even though F1 score has traditionally been adopted in machine learning tasks to evaluate algorithm performance, it emphasizes the agreement of segmentation accuracy including location and border delineation more than the agreement of quantification. For clinical implementation, the cumulative NPA burden has been proven to be a strong biomarker for predicting DR severity.[3] The strong performance of our U-net−based NPA quantification supports its clinical utility as a fully automated tool for measuring total NPA burden and its potential application in biomarker-driven DR risk stratification. If NPI is adopted as a biomarker in future clinical trials, the proposed deep learning algorithm could provide efficient, reproducible, and scalable quantification across large data sets. Because our algorithm performs well in both NPA quantification and NPA localization, it is clinically relevant in the diagnosis and risk stratification of DR.

However, the extension of the FOV in our study to a maximum of 29 × 24 mm presented multiple challenges for accurate NPA segmentation. While 400 kHz swept-source OCT enabled much more expanded FOV with rapid scanning, peripheral defocus artifacts remained more pronounced than smaller FOVs, which predisposes to increased fundus movement.[32] An increased presence of shadow artifacts from eyelashes or vitreous hemorrhage (commonly inferiorly) also makes accurate segmentation of NPA by a deep learning algorithm challenging. Interestingly, our results showed minimal variation in algorithm performance across FOVs ($P = 0.12$). We maintained high segmentation accuracy by using a novel preprocessing pipeline, incorporating en face structural OCT images to enable model recognition and automatic exclusion of NGAs without the need for dedicated ground-truth labels on the structural scan. This improved label quality and algorithm generalizability and reduced false positives that bias the decision boundary of the algorithm toward artifact-correlated features rather than features of true NPA.[33] Previous studies have attempted to reduce the interference of artifacts on NPA analysis by developing a deep learning algorithm to remove shadow artifacts.[26] This was done by superimposing scan data from smaller FOV images to reconstruct artifactual areas. However, this is less applicable for UWF images as nonshadow artifacts such as defocus artifacts also contribute substantially to poor image quality and cannot be removed by such an approach.

Despite the aforementioned challenges, our algorithm performance was observed to improve with increasing DR severity for UWF (29 × 24 mm) images ($P = 0.004$). The F1 scores of mild−moderate, severe NPDR, and PDR were 0.80, 0.82, and 0.86, respectively. In milder DR cases, individual NPAs are scattered across the image. This reduces separability from normally perfused tissue and makes NPA detection more susceptible to artifacts. As DR severity increases, NPAs enlarge and become confluent, acquiring more definitive morphology, thus facilitating differentiation of true NPAs from low-quality regions and artifact-related maskers.

Although there exist other classification systems for grading DR severity, including the "gold standard" ETDRS classification, such classification systems are often not practical for day-to-day clinical practice as they are time-consuming to administer.[34] The ICDR severity scale, on the other hand, is a simplified, clinically oriented system derived from and closely aligned with the ETDRS sevenfield grading protocol, and it forms the basis of various international DR management workflows.[34,35]

In lieu of its widespread use in clinical settings, training our model on ICDR−stratified data sets allows it to be better integrated into existing clinical workflows. It provides rapid automated NPI measurements and reduces interobserver variability, thus making it particularly attractive for DR screening and surveillance. The ICDR severity scale categories also reliably map onto well-defined ETDRS severity group, thus enabling our algorithm and proposed NPI thresholds to be conceptually extrapolated between the 2.[34]

Field of view analysis demonstrated a clear FOV-dependent positive association between NPI and DR severity. Nonperfusion index rose progressively from mild-moderate NPDR to PDR across all 3 scan sizes, and the largest incremental change of NPI was observed in 29 × 24 mm. Notably, the 29 × 24 mm scan was the only FOV in which all pairwise comparisons of DR severity were significant on Dunn test. This suggests that discriminative performance improves with increasing FOV. As the 29 × 24 mm scan extends into the peripheral retina, these findings imply that peripheral regions contribute disproportionately to the overall NPA burden, which is particularly informative for distinguishing advanced DR stages. This is consistent with UWF FFA studies reporting that >70% of NPA lies outside the posterior pole[10] and that peripheral NPA increases markedly with advancing DR stage.[30] Among the 3 FOVs utilized in our study, the UWF 29 × 24 mm scans also demonstrated the largest increment in NPI across DR severities, underscoring the value of UWF SS-OCTA for detecting peripheral ischemia that is often missed by conventional macular protocols. In contrast, the smaller area of the 6 × 6 and 12 × 12 mm scans likely accounts for the lower absolute NPI values and weaker interstage differences observed.

Taken together, these data support the complementary use of UWF OCTA to enhance detection and monitoring of ischemic changes in DR. Furthermore, our U-net–based segmentation algorithm provides an efficient and scalable approach to quantify NPA across these large-area data sets, improving analytical productivity and reproducibility.

Our deep learning algorithm also performed well for FAZ segmentation with an F1 score of 0.88 ± 0.05 for 6 × 6 mm and 0.85 ± 0.05 for 12 × 12 mm. This is comparable to the results published by Le Boite et al, reporting a F1 score of 0.879 for FAZ segmentation on 15 × 15 mm images. Interestingly, we note significant differences in algorithm performance between mild–moderate NPDR (F1 = 0.93) and PDR (F1 = 0.81) on 6 × 6 mm images. This could be explained by increased FAZ circularity with worsening DR severity which makes FAZ morphology less distinct in PDR compared with mild–moderate NPDR.[36] However, previous studies have demonstrated significant variation in FAZ area even in healthy controls, which limits the utility of FAZ as a biomarker for predicting DR progression.[37] Furthermore, peripheral NPA has been shown to correlate more strongly with DR severity than FAZ area, and studies have reported that posterior pole perfusion can be preserved in eyes with advanced DR.[38,39]

Our study demonstrates that NPA is a robust biomarker that correlates strongly with DR severity across 3 different FOV. Prior work has also shown that peripheral NPA underlies predominantly peripheral lesions, which are linked to more advanced disease than ETDRS grading alone would suggest.[40,41] In routine practice, however, NPA assessment has been constrained by the invasive, time-consuming nature of FFA and the labor-intensive manual segmentation it requires. In contrast, UWF OCTA provides rapid, dye-free, high-resolution visualization of the retinal microvasculature across multiple FOV and is more amenable to repeated imaging. By automating OCTA-derived NPA quantification, our deep learning algorithm further reduces grader burden and interobserver variability, markedly improving the efficiency and consistency of NPI-based staging. Its rapid processing makes it well suited for busy eye clinics and screening program to quantify ischemic burden, guide timely management decisions, and support longitudinal monitoring. In addition, its high throughput and reproducibility also makes NPA a potentially attractive biomarker for clinical trials that need to evaluate large imaging data sets.

Limitations of this study include smaller sample size derived from a single center. Ultra-widefield SS-OCTA also has longer scan times compared with ordinary SS-OCTA FOVs, resulting in a greater tendency for poor patient cooperation and artifact generation. This reduces image quality and makes obtaining sufficient good quality scans for algorithm training challenging. Future work will expand to larger samples from multicenter cohorts, which is essential for validating model robustness across diverse data and imaging environments. Secondly, establishing ground-truth NPA segmentation remains challenging. Our group has incorporated automated detection of shadow and other artifact types into the algorithm, coupled with a majority-voting strategy to reduce intergrader variability in defining true flow absence and NGA. While shadow artifacts can be reliably identified using corresponding structural OCT scans, other sources of image degradation—such as defocus, segmentation errors, and pupil vignetting—remain more challenging to delineate consistently and exhibit higher intergrader variability. Furthermore, defocus artifacts tend to arise more frequently in the periphery of UWF SS-OCTA angiograms due to the greater depth-of-focus of swept-source scanning. Moving forward, we aim to establish a comprehensive artifact classification and image quality scoring framework to stratify algorithm performance across different image qualities, further enhancing the robustness of automated NPA segmentation on UWF SS-OCTA. Continued advancements in UWF OCTA acquisition technology to minimize these inherent image quality limitations will likewise improve algorithm performance and expand its clinical utility. In addition, given that our study is a cross-sectional study, we have only evaluated the efficacy of NPI as a biomarker in a single frame. Future studies could implement automatic NPA segmentation to follow-up a cohort of patients with DR to establish the utility of NPI in DR monitoring.

Another limitation is that the algorithm was trained on the ARL. While the ARL provides a comprehensive visualization of retinal nonperfusion, we acknowledge the unique diagnostic insights that individual vascular plexuses, such as the superficial and deep capillary layers, may provide. Future work will include layer-specific analyses to better understand the relative contributions of each plexus to DR detection and progression.[15]

Additionally, as our algorithm is focused primarily on generalized detection of NPA, it is unable to distinguish if NPA is purely from DR or from other ischemic retinopathies. However, the results of our covariate analysis have shown that patient comorbidities such as hypertension and hyperlipidemia do not confound the relationship between NPI and DR severity. This supports the internal validity of NPI as a marker of DR progression. Yet, because NPA is a manifestation of multiple ischemic retinopathies, this suggests potential applicability of the algorithm to other disease, such as retinal vascular occlusion. Future studies will evaluate algorithm performance in NPA detection across other conditions.

Furthermore, although Bland–Altman analysis showed strong agreement between algorithm-predicted NPI and ground truth, supporting the clinical relevance of the algorithm and its potential for application, there is no clear threshold to assess its clinical utility and feasibility for diagnosis and prognostication of DR. Determining a threshold is also challenging due to interclinician variability of what is considered acceptable accuracy. Bogost et al[42] previously suggested that semi-automated algorithms involving human modification of automated NPA segmentation could be explored on top of fully automated algorithms such as ours to improve the quantification potential for clinical adoption. Hence, a solution to this limitation could be to directly compare the performance of our fully automated algorithm with semi-automated algorithms to determine whether human modification significantly improves NPA quantification by a deep learning algorithm.

In summary, this study presents an artifact-aware deep learning framework for automated identification and quantification of retinal nonperfusion on single-scan UWF SS-OCTA. The algorithm efficiently delivers accurate, reproducible NPA segmentation across different FOVs, enabling robust NPI measurement without compromising performance. This scalability makes OCTA-derived NPI a promising biomarker for large-volume DR screening and a potential quantitative endpoint for assessing treatment response and disease progression in clinical trials.

Footnotes and Disclosures

Originally received: October 13, 2025.
Final revision: December 6, 2025.
Accepted: December 22, 2025.
Available online: January 5, 2026. Manuscript no. XOPS-D-25-00874.

[1] Lee Kong Chian School of Medicine, Nanyang Technological University, Singapore.

[2] Ophthalmology Department, Tan Tock Seng Hospital, National Healthcare Group Eye Institute, Singapore.

[3] Research and Development Department, MedPath AI, Singapore.

[4] Eye and ENT Hospital of Fudan University, Shanghai, China.

[5] Singapore Eye Research Institute, Singapore.

[6] Duke-NUS Medical School, Singapore.

[7] Yong Loo Lin School of Medicine, National University of Singapore, Singapore.

[8] Casey Eye Institute, Oregon Health & Science University, Portland, USA.

[9] Department of Biomedical Engineering, Oregon Health and Science University, Portland, Oregon.

*T.Y.L. and J.S. are joint first authors.

Disclosures:

The Article Publishing Charge (APC) for this article was paid by Tan Tock Seng Hospital.

All authors have completed and submitted the ICMJE disclosures form.

We would like to acknowledge the National Healthcare Group Centre for Medical Technologies & Innovation (MedTech) Grant, the Ng Teng Fong Healthcare Innovation Programme (HIP) and the Digital Prototyping Budget (DPB) grant co-funded by Tan Tock Seng Hospital and Ng Teng Fong General Hospital, as sources of funding for our project.

The authors made the following disclosures:

Y.J.: Grants − Novartis, Carl Zeiss Meditec; Royalties − Visionix/Optovue, Inc, Genentech; Consultant − Boeringer Ingelheim Inc., Carl Zeiss Meditec, Abbvie, Annexon, Apellis, Bayer, Character Biosciences, Eyepoint Pharmaceuticals, Genentech/Roche, InflammX, Occudyne, OD-OS MacuTherm GmbH, Regeneron, Unity Biotechnology, Valitor; Honoraria − Visionix/Optovue, Inc, Genentech, Optos Inc; Stock or stock options − IFOCUS IMAGING, Apellis, Character Biosciences, InflammX, Occudyne, Valitor.

S.W.Z.: Grants − Intalight.

HUMAN SUBJECTS: Human subjects were included in this study. This study was approved by the Institutional Review Board of Tan Tock Seng Hospital and adheres to the Declaration of Helsinki. Written informed consent was obtained from all patients.

No animal subjects were used in this study.

Author Contributions:

Conception and design: Zhou, Song, Loh, Sia

Analysis and interpretation: Loh, Sia, Zhou, Zhuang, Seah, Song, Jia, Agrawal

Data collection: Loh, Sia, Seah, Zhuang, Song, Qiu, Shen, Yu, Tan, Tang, Asad, C.M.H. Goh, Ang, Chng, Lo, Paniharam, S.K. Goh, Oo, Wang, Gan, Zhou

Obtained funding: Zhou

Overall responsibility: Loh, Sia, Song, Zhou

Abbreviations and Acronyms:
ARL = all-retinal layer; **DR** = diabetic retinopathy; **FAZ** = foveal avascular zone; **FFA** = fundus fluorescein angiography; **FOV** = field of view; **ICC** = intraclass correlation coefficient; **ICDR** = International Clinical Diabetic Retinopathy; **LOA** = limits of agreement; **NGA** = nongradable area; **NPA** = nonperfusion area; **NPDR** = nonproliferative diabetic retinopathy; **NPI** = nonperfusion index; **OCTA** = OCT angiography; **PDR** = proliferative diabetic retinopathy; **UWF** = ultra-widefield; **UWF SS-OCTA** = ultra-widefield swept source OCT angiography.

Keywords:
Diabetic retinopathy, Nonperfusion area (NPA), Nonperfusion index (NPI), Deep learning, Convolutional neural network (CNN), Automated image analysis, Biomarkers, Foveal avascular zone (FAZ) and artificial intelligence in ophthalmology, Ultra-widefield swept-source optical coherence tomography angiography (UWF SS-OCTA).

Correspondence:
Sandy Wenting Zhou, Department of Ophthalmology, Tan Tock Seng Hospital, National Health Group Eye Institute, 11 Jalan Tan Tock Seng, Singapore 308433. E-mail: Sandy_W_Zhou@nhghealth.com.sg.

References

1. Teo ZL, Tham YC, Yu M, et al. Global prevalence of diabetic retinopathy and projection of burden through 2045: systematic review and meta-analysis. *Ophthalmology*. 2021;128:1580−1591.
2. Kropp M, Golubnitschaja O, Mazurakova A, et al. Diabetic retinopathy as the leading cause of blindness and early predictor of cascading complications—risks and mitigation. *EPMA J*. 2023;14:21−42.
3. Silva PS, Dela Cruz AJ, Ledesma MG, et al. Diabetic retinopathy severity and peripheral lesions are associated with nonperfusion on ultrawide field angiography. *Ophthalmology*. 2015;122:2465−2472.
4. Ruia S, Tripathy K. Fluorescein angiography. In: StatPearls. StatPearls Publishing. http://www.ncbi.nlm.nih.gov/books/NBK576378/; 2025. Accessed November 26, 2025.
5. Jia Y, Bailey ST, Hwang TS, et al. Quantitative optical coherence tomography angiography of vascular abnormalities in the living human eye. *Proc Natl Acad Sci U S A*. 2015;112:E2395−E2402.
6. Hwang TS, Gao SS, Liu L, et al. Automated quantification of capillary nonperfusion using optical coherence tomography angiography in diabetic retinopathy. *JAMA Ophthalmol*. 2016;134:367−373.

7. Hwang TS, Jia Y, Gao SS, et al. Optical coherence tomography angiography features of diabetic retinopathy. *Retina*. 2015;35:2371−2376.
8. Garg I, Uwakwe C, Le R, et al. Nonperfusion area and other vascular metrics by wider field swept-source OCT angiography as biomarkers of diabetic retinopathy severity. *Ophthalmol Sci*. 2022;2:100144.
9. Jia Y, Hormel TT, Hwang TS, et al. Widefield OCT angiography. *Prog Retin Eye Res*. 2025;107:101378.
10. Silva PS, Liu D, Glassman AR, et al. Assessment of fluorescein angiography nonperfusion in eyes with diabetic retinopathy using ultrawide field retinal imaging. *Retina*. 2022;42:1302−1310.
11. Guo Y, Camino A, Wang J, et al. MEDnet, a neural network for automated detection of avascular area in OCT angiography. *Biomed Opt Express*. 2018;9:5147.
12. Guo Y, Hormel TT, Xiong H, et al. Development and validation of a deep learning algorithm for distinguishing the nonperfusion area from signal reduction artifacts on OCT angiography. *Biomed Opt Express*. 2019;10:3257.
13. Wang J, Hormel TT, You Q, et al. Robust non-perfusion area detection in three retinal plexuses using convolutional neural network in OCT angiography. *Biomed Opt Express*. 2020;11:330.
14. Guo Y, Hormel TT, Gao L, et al. Quantification of nonperfusion area in montaged widefield OCT angiography using deep learning in diabetic retinopathy. *Ophthalmol Sci*. 2021;1:100027.
15. Guo Y, Hormel TT, Gao M, et al. Multi-plexus nonperfusion area segmentation in widefield OCT angiography using a deep convolutional neural network. *Trans Vis Sci Tech*. 2024;13:15.
16. Nagasato D, Tabuchi H, Masumoto H, et al. Automated detection of a nonperfusion area caused by retinal vein occlusion in optical coherence tomography angiography images using deep learningZhang J, ed. *PLoS One*. 2019;14:e0223965.
17. Hormel TT, Beaulieu WT, Wang J, et al. Artificial intelligence versus rules-based approach for segmenting NonPerfusion area in a DRCR retina network optical coherence tomography angiography dataset. *Invest Ophthalmol Vis Sci*. 2025;66:22.
18. Zhang M, Hwang TS, Campbell JP, et al. Projection-resolved optical coherence tomographic angiography. *Biomed Opt Express*. 2016;7:816−828.
19. Anvari P, Ashrafkhorasani M, Habibi A, Falavarjani KG. Artifacts in optical coherence tomography angiography. *J Ophthalmic Vis Res*. 2021;16:271−286.
20. Mahapatra SK, Mohanty A, Bidasaria A, Parhi A. Comparison of swept source − optical coherence tomography angiography with fundus fluorescein angiography for detection of lesions in diabetic retinopathy. *Taiwan J Ophthalmol*. 2025;15:443−449.
21. Guo C, Xiao N, Li F, et al. Comparison of widefield swept-source optical coherence tomography angiography and ultra-widefield fluorescein angiography in the detection of non-perfusion areas in diabetic retinopathy. *Front Endocrinol*. 2025;16:1521837.
22. Zhao Z, Huang S, Zhang W, et al. Automated interpretation of fundus fluorescein angiography with multi-retinal lesion segmentation. *medRxiv*. posted online December 21, 2024:2024.12.20.24319428.
23. Feng W, Wang B, Song D, et al. Development and evaluation of a deep learning model for automatic segmentation of nonperfusion area in fundus fluorescein angiography. *J Big Data*. 2024;11:131.
24. Le Boité H, Bonnin S, Gallardo M, et al. Deep learning for retinal non-perfusion and foveal avascular zone analysis in widefield OCTA in diabetic retinopathy. *Sci Rep*. 2025;15:30225.
25. Cui Y, Zhu Y, Wang JC, et al. Imaging artifacts and segmentation errors with wide-field swept-source optical coherence tomography angiography in diabetic retinopathy. *Transl Vis Sci Technol*. 2019;8:18.
26. Gao M, Guo Y, Hormel TT, et al. Reconstruction of high-resolution 6×6-mm OCT angiograms using deep learning. *Biomed Opt Express*. 2020;11:3585−3600.
27. Ho J, Dans K, You Q, et al. Comparison of 3×3 mm versus 6×6 mm optical coherence tomography angiography scan sizes in the evaluation of non-proliferative diabetic retinopathy. *Retina*. 2019;39:259−264.
28. Wang XN, Cai X, Li SW, et al. Wide-field swept-source OCTA in the assessment of retinal microvasculature in early-stage diabetic retinopathy. *BMC Ophthalmol*. 2022;22:473.
29. Zeng Y, Liu M, Li M, et al. Early changes to retinal structure in patients with diabetic retinopathy as determined by ultra-wide swept-source optical coherence tomography-angiography. *Front Endocrinol*. 2023;14:1143535.
30. Zhang J, Huo Q, Xia D, et al. Advances in application of swept-source optical coherence tomography angiography in diagnosis and treatment of diabetic retinopathy. *Front Ophthalmol (Lausanne)*. 2023;3:1116391.
31. Russell JF, Al-khersan H, Shi Y, et al. Retinal non-perfusion in proliferative diabetic retinopathy before and after panretinal photocoagulation assessed by wide field OCT angiography. *Am J Ophthalmol*. 2020;213:177−185.
32. De Pretto LR, Moult EM, Alibhai AY, et al. Controlling for artifacts in widefield optical coherence tomography angiography measurements of non-perfusion area. *Sci Rep*. 2019;9:9096.
33. Karimi D, Dou H, Warfield SK, Gholipour A. Deep learning with noisy labels: exploring techniques and remedies in medical image analysis. *Med Image Anal*. 2020;65:101759.
34. Yang Z, Tan TE, Shao Y, et al. Classification of diabetic retinopathy: past, present and future. *Front Endocrinol (Lausanne)*. 2022;13:1079217.
35. Attiku Y, Nittala MG, Velaga SB, et al. Comparison of diabetic retinopathy severity grading on ETDRS 7-field versus ultrawide-field assessment. *Eye*. 2023;37:2946−2949.
36. Yang Q, Teo KYC, Hong Y, et al. Flow and ischemic changes in retina and choroid across diabetic retinopathy spectrum: a SS-OCTA study. *Eye*. 2025;39:1631−1640.
37. Wang X, Han Y, Sun G, et al. Detection of the microvascular changes of diabetic retinopathy progression using optical coherence tomography angiography. *Trans Vis Sci Tech*. 2021;10:31.
38. Yasukura S, Murakami T, Suzuma K, et al. Diabetic nonperfused areas in macular and extramacular regions on widefield optical coherence tomography angiography. *Invest Ophthalmol Vis Sci*. 2018;59:5893−5903.
39. Konno A, Ishibazawa A, De Pretto L, et al. Relationship between nonperfusion area from widefield optical coherence tomography angiography and macular vascular parameters in diabetic retinopathy. *Int Ophthalmol*. 2023;43:4803−4814.
40. Silva PS, Marcus DM, Liu D, et al. Association of ultra-widefield fluorescein angiography−identified retinal nonperfusion and the risk of diabetic retinopathy worsening over time. *JAMA Ophthalmol*. 2022;140:936.
41. Marcus DM, Silva PS, Liu D, et al. Association of predominantly peripheral lesions on ultra-widefield imaging and the risk of diabetic retinopathy worsening over time. *JAMA Ophthalmol*. 2022;140:946.
42. Bogost J, Linderman RE, Slater R, et al. Longitudinal comparison of geographic atrophy enlargement using manual, semiautomated, and deep learning approaches. *Ophthalmol Sci*. 2025;5:100787.